Article

Synthetic Smectite Colloids: Characterization of Nanoparticles after Co-Precipitation in the Presence of Lanthanides and Tetravalent Elements (Zr, Th)

Muriel Bouby *, Nicolas Finck † and Horst Geckeis †

Karlsruhe Institute of Technology (KIT) - Campus North (CN), Institute for Nuclear Waste Disposal (INE), Hermann-von Helmholtz-Platz 1, D-76344 Eggenstein-Leopoldshafen, Germany;
E-Mails: nicolas.finck@kit.edu (N.F.); horst.geckeis@kit.edu (H.G.)

†   These authors contributed equally to this work.

*   Author to whom correspondence should be addressed; E-Mail: muriel.bouby@kit.edu;
Tel.: +49-721-608-2-4939; Fax: +49-721-608-2-3927.

Abstract: The magnesian smectite hectorite is a corrosion product frequently detected in nuclear waste glass alteration experiments. The structural incorporation of a single trivalent lanthanide was previously demonstrated. Hectorite was presently synthesized, for the first time, in the presence of several lanthanides (La, Eu, Yb) following a multi-step synthesis protocol. The smallest-sized particles (nanoparticles, NPs) were isolated by centrifugation and analyzed by asymmetrical flow field-flow fractionation (AsFlFFF) coupled to ICP-MS, in order to obtain information on the elemental composition and distribution as a function of the size. Nanoparticles can be separated from the bulk smectite phase. The particles are able to accommodate even the larger-sized lanthanides such as La, however, with lower efficiency. We, therefore, assume that the incorporation proceeds by substitution for octahedral Mg accompanied by a concomitant lattice strain that increases with the size of the lanthanides. The presence of a mixture does not seem to affect the incorporation extent of any specific element. Furthermore, syntheses were performed where in addition the tetravalent zirconium or thorium elements were admixed, as this oxidation state may prevail for many actinide ions in a nuclear waste repository. The results show that they can be incorporated as well.

1. Introduction

Vitrified high level nuclear waste (HLW) placed in steel canisters is considered as an appropriate, long-term stable waste form for disposal in deep geological repositories. Over geological time scales, (ground) water intrusion cannot be neglected, resulting in possible canister failure and, ultimately, glass corrosion. Earlier laboratory studies simulating the alteration of HLW glass have identified numerous corrosion products, the nature of which depends on the initial source, *i.e.*, the glass formulation and the water composition [1]. The presence of radionuclides (RNs) during the formation of such corrosion products in aqueous environments opens the possibility of a structural retention, thus leading to an efficient retention mechanism. However, the potential release of colloidally-stable nanoparticulates from those alteration layers represents a potential RN migration vector. Clay nanoparticles have been identified as secondary phases in the glass alteration layer [2,3] and were characterized as partially-crystalline smectite [4]. Due to their small size and relatively high surface area, partly induced by isomorphic substitution, smectite clay particles are known to exhibit high colloidal stability depending on given groundwater conditions.

The magnesian smectite hectorite has been detected in the glass alteration layer [5–7]. Some studies reported hectorite syntheses in the presence of the trivalent actinide curium [8,9] or of its non-radioactive chemical surrogate europium [10] following a multi-step synthesis protocol using brucite as a precursor phase [11]. For these cations, luminescence spectroscopy data suggested the incorporation in the bulk structure from the early stage synthesis. X-ray absorption spectroscopy (XAS) experiments have also been performed for hectorite crystallized in the presence of lutetium [12], europium [13] or americium [14]. Structural data such as coordination numbers and bond lengths were consistent with a location of the trivalent lanthanide (Ln) / actinide (An) in an octahedral environment into the precursor phase and in the final crystalline smectite product. Significant differences in the chemical environment of the different metal ions with different ionic radii were not observed. The studies concluded that the incorporation is only possible by substituting for Mg at octahedral site with concomitant distortion of the structure around the substituted element because of the size mismatch [15] with cations typically occurring at clay octahedral site (e.g., $r(^{VI}Mg(II)) = 0.72$ Å, $r(^{VI}Li(I)) = 0.76$ Å, $r(^{VI}Fe(III)) = 0.65$ Å, $r(^{VI}Fe(II)) = 0.78$ Å). Nevertheless, those studies provided a proof of principle that large cations can be incorporated into the clay crystal structure.

Recent studies reported the analysis of the stable nanoparticles (NPs) fraction of a hectorite suspension synthesized in the presence of Lu or Eu [13,16]. The NPs were separated from the "bulk" suspension by centrifugation and analyzed by application of the asymmetrical flow field-flow fractionation (AsFlFFF) method coupled to an ICP-MS detector. AsFlFFF is a chromatographic-like technique used to separate particles according to their size. Hyphenation to sensitive analytical techniques such as ICP-MS allows the simultaneous determination of the corresponding elemental compositions. The coupling to sensitive detection techniques was first reported in 1992 [17] and is

intensively used nowadays [18–23] in various fields such as food science and technology [24], pharmaceutical, biomedical, biological and toxicological analysis [25–30], and in environmental engineering science [16,31–53].

In an earlier investigation [13], we showed that the AsFlFFF/ICP-MS characterization of a suspension containing hectorite NP synthesized in the presence of Eu was consistent with the results of the XAS analysis of the bulk. This indicates that NPs and bulk hectorite material had similar structures and compositions and demonstrates that the NPs extracted from the bulk can be considered as miniatures of the macrocrystallites.

In all reported studies so far, only one element was used in the hectorite co-precipitation experiments and information on the chemical environment was obtained by application of element-specific spectroscopic techniques, such as time-resolved laser-induced fluorescence spectroscopy (TRLFS) or XAS [8,10,12]. However, upon HLW glass corrosion, numerous RN of various sizes and oxidation states will be released and, thus, possibly be present during the neo-formation of the secondary phases. Naturally occurring clay minerals, such as the Fe-rich smectite nontronite from Eolo Sea mount [54] or the mixed-layer illite-smectite from the sedimentary Bowen basin (Australia) [55], contain the whole series of lanthanides and their content is dependent on the ionic radius, meaning that the clays are enriched in heavier (*i.e.*, smaller) elements [56]. In order to verify whether the ionic radii have a similar impact on trace element incorporation in natural clays as for the laboratory synthesis route, we crystallized hectorite from a brucite precursor phase, precipitated in the presence of La, Eu, and Yb. Separately, hectorite is synthesized once again in the simultaneous presence of La, Eu, Yb and with, in addition, as a preliminary investigation, tetravalent elements Zr(IV) or Th(IV) to test their possible incorporation. The NPs were isolated from the bulk by centrifugation and analyzed by AsFlFFF coupled to ICP-MS in order to investigate the influence of the cation size on the incorporation.

2. Experimental Section

2.1. Hectorite Synthesis and Nanoparticles Separation

All samples were prepared using ultra-pure water (Milli-Q system (Millipore), 18.2 MΩ·cm) and reagents of ACS grade or higher. Stock solutions of individual lanthanide ([La] = 102 mmol.L^{-1}, [Eu] = 95 mmol.L^{-1}, [Yb] = 49 mmol.L^{-1}) were prepared by dissolving the corresponding oxide (La_2O_3, Eu_2O_3 or Yb_2O_3, all from Alfa Aesar, Reacton 99.999% (REO)) in 2% $HClO_4$. The sources of Zr and Th were $ZrO(NO_3)_2 \cdot H_2O$ (Aldrich) and $ThCl_4$ dissolved in 1 M HCl and 0.93 M HCl, respectively, to obtain final stock solutions concentrations of [Zr] = 79 µmol.L^{-1} and [Th] = 41 mmol.L^{-1}. $MgCl_2 \cdot 6H_2O$, LiF or LiOH and Si sol Ludox HS-30 (Aldrich) were used for the hectorite crystallization.

Hectorite containing La, Eu and Yb (sample 3LnCopHec) was synthesized following a multi-step synthesis protocol described in previous studies [10] and adapted from a procedure developed earlier [11]. Brucite was first precipitated in the presence of the three lanthanides. For that, 32 mmol Mg were dissolved in ultra-pure water (~200 mL), the individual lanthanides were added (47.7 µmol La, 45.7 µmol Eu and 64.4 µmol Yb) and brucite was precipitated under vigorous stirring by adding 2 M NH_4OH (pH final ~9.5). The suspension was then centrifuged (45 min at ~2100 g, Megafuge 2.0 R, Thermo Scientific, Heraeus Instrument) and the supernatant discarded. The lanthanide content in the supernatant

was not quantified. Nevertheless, at this pH the lanthanide solubility is low and earlier luminescence data for Cm [8] indicated that >99% of the initially added actinide was structurally incorporated in the brucite precursor and that ~50% of the Cm(III) remained structurally incorporated after hectorite cristallisation, while the rest stayed surface adsorbed. Thus, we assume that they are quantitatively associated (adsorbed or incorporated) with brucite. This brucite precursor was then thoroughly washed with ultra-pure water in several centrifugation cycles. The resulting slurry was refluxed in the presence of LiF in an oil bath for 30 min, the Si sol (48 mmol Si) was added and the suspension was left to react under reflux for 3 days. After cooling, the synthetic clay suspension was centrifuged, the supernatant discarded and shortly washed at pH 3 (HCl) to remove any unreacted precursor that may be present, and finally thoroughly washed again with ultra-pure water. The hectorite is kept in ultra-pure water.

Hectorite containing La, Eu, Yb, and Zr, sample 3LnZrCopHec, was synthesized similarly. Brucite was first precipitated in the presence of all the elements. For that, 23.8 mmol Mg were dissolved in ultra-pure water (~400 mL), then the individual elements were added (35.2 µmol La, 33.7 µmol Eu, 47.5 µmol Yb, 23.7 µmol Zr and 1.2 mmol Li). The brucite was precipitated under vigorous stirring by adding quickly 10 M NaOH (pH final ~11). Immediately after, this precursor was thoroughly washed with ultra-pure water in several centrifugation cycles. The resulting slurry was refluxed in the presence of LiF (6.3 mmol Li) in an oil bath for 30 min, the Si sol (36.0 mmol Si) was added to crystallize the smectite and the suspension was left to react under reflux for 3 days. After cooling, the synthetic clay suspension was centrifuged, the supernatant discarded and shortly washed at pH 3 (HCl) to remove any unreacted precursor that may be present and, finally, thoroughly washed again with ultra-pure water. Hectorite containing La, Eu, Yb, and Th, sample 3LnThCopHec, was synthesized similarly using the following amounts: 16.0 mmol Mg, 23.8 µmol La, 22.8 µmol Eu, 32.2 µmol Yb, 18.7 µmol Th and 1.1 mmol Li mixed in solution to precipitate the brucite precursor (pH final ~10). 4.3 mmol Li and 24.5 mmol Si were then added to crystallize the smectite. The brucite washing, hectorite crystallization and final clay washing were identical.

The mineralogical characterization of the synthetic hectorite samples was determined by X-ray diffraction. Data were collected with a D8 Advance (Bruker) diffractometer (Cu Kα radiation) equipped with an energy-dispersive detector (Sol-X). An example of XRD pattern collected for the hectorite synthesized in the presence of La, Eu, Yb, and Th, and prepared as an oriented sample, is shown in the Appendix. Only smectite could be detected on the diffractogram; no other (crystalline) phase could be evidenced, *i.e.*, no brucite precursor phase was detected. The presence of trace amounts of dopants, thus, did not affect the smectite synthesis procedure.

The NPs were separated from the "bulk" particles by centrifugation of 15 mL homogeneous suspension for 35 min at ~2700 g (Megafuge 2.0 R, Thermo Scientific, Heraeus Instrument). The resulting supernatants containing the NPs had pH values of 8.2 (3LnCopHec-sup), 8.0 (3LnZrCopHec-sup) or 8.5 (3LnThCopHec-sup) and were kept in contact with the settled solid until analysis. The repeatability of this separation protocol has already been checked [13,16]. The Mg, La, Eu, Yb, Zr, and Th concentrations were determined during AsFlFFF/ICP-MS experiments and the Mg/Si molar ratio from separate ICP-OES (Optima 2000 DV) measurements (Table 1). Compared to the theoretical value of Mg/Si = 0.67, the molar ratio indicates that the Si is in excess in the present hectorite syntheses and is assigned to the presence of amorphous Si [57].

Table 1. Elemental composition and Mg/Si molar ratio of the supernatant before dilution for AsFlFFF analysis.

Element (Ionic radii r^{VI} [15]) / Sample	Mg (0.72 Å)	La (1.03 Å)	Eu (0.95 Å)	Yb (0.87 Å)	Zr (0.72 Å)	Th (0.94 Å)	Mg:Si (mol:mol)
3LnCopHec-sup							
mg.L^{-1}	72 ± 4	0.71 ± 0.01	0.81 ± 0.01	1.13 ± 0.01	-	-	0.50 ± 0.02
mmol.L^{-1}	3.0 ± 0.2	0.0051 ± 0.0001	0.0053 ± 0.0001	0.0065 ± 0.0001			
3LnZrCopHec-sup							
mg.L^{-1}	49 ± 3	0.48 ± 0.02	0.95 ± 0.04	1.5 ± 0.1	0.7 ± 0.1	-	0.32 ± 0.02
mmol.L^{-1}	2.0 ± 0.1	0.0034 ± 0.0001	0.0063 ± 0.0001	0.0087 ± 0.0005	0.008 ± 0.001		
3LnThCopHec-sup							
mg.L^{-1}	2629 ± 40	22.5 ± 0.3	26.6 ± 0.3	33.9 ± 0.4	-	40.2 ± 0.5	0.57 ± 0.02
mmol.L^{-1}	108 ± 2	0.162 ± 0.002	0.175 ± 0.002	0.196 ± 0.002		0.173 ± 0.002	

Before injection into the AsFlFFF system, the supernatant is diluted with the eluent (ultra-pure water at pH 9.3 by addition of NaOH) to reach 10–15 mg.L^{-1} Mg.

2.2. Asymmetric Flow Field-Flow Fractionation (AsFlFFF) coupled to MALLS/ICP-MS Detectors

The flow field-flow fractionation method is well-established and the reader is referred to [58,59] for the theoretical background. Examples of AsFlFFF application to investigate modes of lanthanide interaction with clay minerals can be found in [13,16,39].

As the equipment used in this study (HRFFF 10.000 A4F, Postnova analytics, Landsberg, Germany) has already been described in details in [39,60], only a brief description is given here. The suspension (solid (nano)particles suspended in a liquid phase) is injected into a thin, ribbon-like channel delimited by a PTFE spacer having a thickness of 500 μm, and the sample components (*i.e.*, NPs) are eluted by a carrier solution. The carrier solution is ultra-pure water adjusted to pH 9.3 by the addition of ultra-pure NaOH (Merck, Germany), and is degassed prior to use in a vacuum degasser (PN7505 Vacuum Degasser, Postnova Analytics, Landsberg, Germany). Inside the channel, the carrier flow has a laminar parabolic profile and is under the action of a cross-flow (secondary perpendicularly applied flow field). This drives the components to the accumulation wall which is covered by an ultra-filtration membrane made of regenerated cellulose (5 kDa). This membrane retains sample components larger than the nominal molecular weight cut-off within the channel. The diffusion of the components back into the channel counterbalances the cross-flow. Particles with higher diffusion rates reach faster flow streamlines and are eluted more rapidly. In the "normal" elution mode, see Figure 1-I, smaller particles having higher diffusion rates are eluted ahead of larger ones. In the "steric" elution mode, see Figure 1-II, larger particles are eluted prior to smaller ones because they protrude into the higher-velocity flow streams located away from the channel walls [59]. Consequently, by injecting a suspension with a multimodal size distribution (*i.e.*, a suspension having nanoparticles of various sizes), large particles eluted in steric mode cannot be unambiguously distinguished from smaller particles eluted in normal mode. Small particles can be mixed up with larger ones, or vice versa, as both might be eluted

simultaneously. However, the ambiguity can, for example, be lifted up by analyzing the effluent by laser light scattering (LLS) particularly sensitive to larger particles.
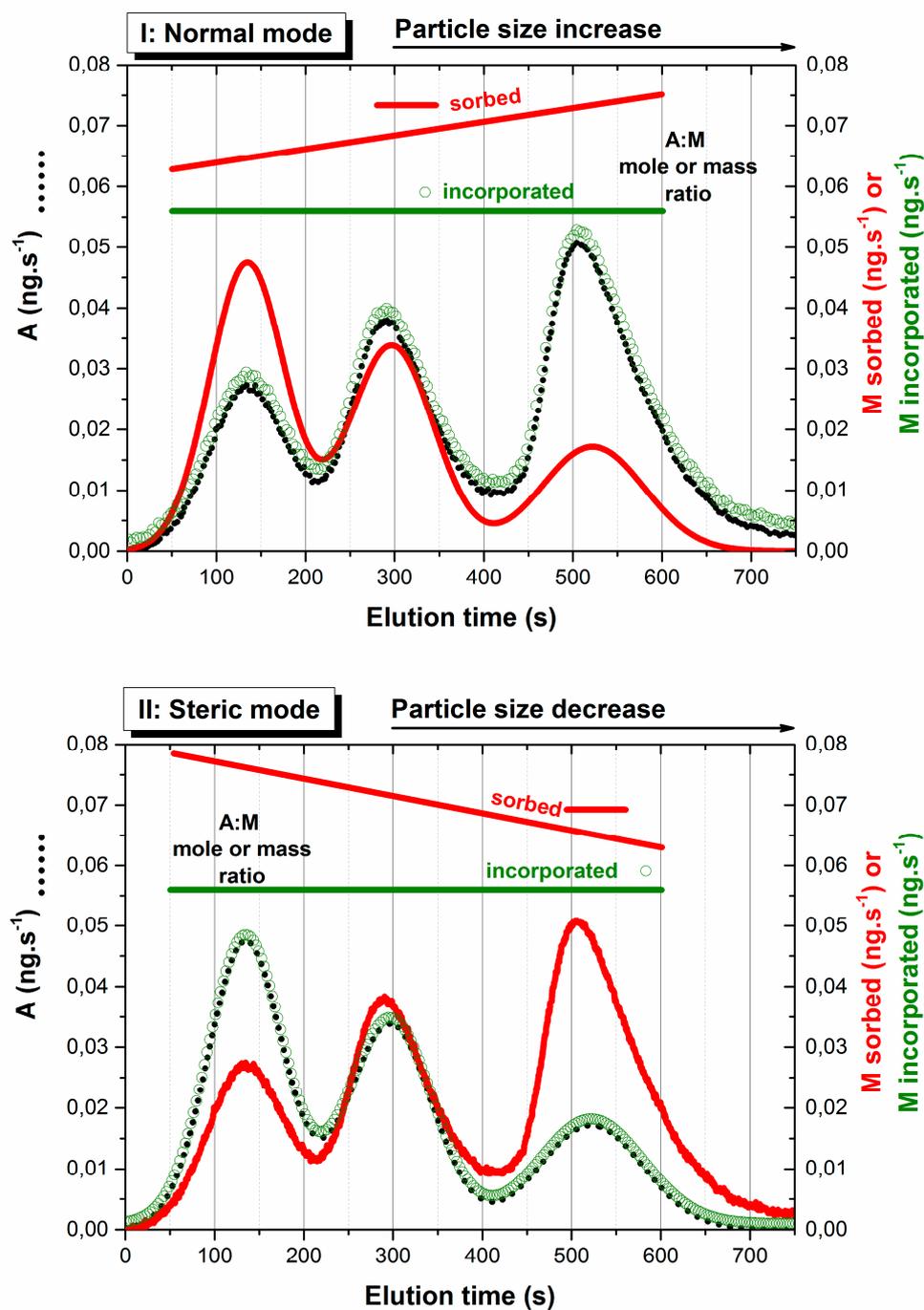
Figure 1. ICP-MS fractograms (upper part: normal elution mode, lower part: steric elution mode) corresponding to a NPs suspension having a multimodal size distribution where A is a main structural constituent (black dots) and M a trace component interacting either by surface adsorption (M sorbed, red line) or by structural incorporation (M incorporated, green dots) in the particles. Resulting A/M ratios are indicated above the fractograms.

After fractionation, the effluent is first directed to a UV-VIS spectrophotometer (LambdaMax LC Modell 481, Waters, Milford, USA) and to a multi-angle laser light-scattering (MALLS) detector. For the MALLS detection, a 5 mW HeNe laser provides the incident light beam (λ_{em} = 632 nm) that is directed through the detector cell of 70 µL volume. The scattered light is detected by an array of 18 photodiodes arranged at different angles relative to the incoming laser beam. The detection is performed by a commercial DAWN-DSP-F light-scattering photometer (Wyatt Technology Corp., Santa Barbara, USA). After the LLS detection, the effluent is mixed with 6% HNO$_3$ containing Rh as internal standard at a constant flow rate of 0.5 mL.min^{-1} using a HPLC pump (Smartline Pump 1000, Knauer, Germany) via a T-piece and then introduced into the cross-flow type nebulizer of an ICP-MS (X-Series2, Thermo Scientific, Germany). The HPLC pump is equipped with an injection/switching valve (Knauer, Germany) and two injection loops (100 mL or 2.8 mL volume) which are used to inject standard solutions, in order to quantify the sample recovery and for concentration quantification. In this work, the laminar outflow rate is adjusted nominally to 0.4 mL.min^{-1} and the cross-flow rate is programmed to decrease linearly from 0.27 mL.min^{-1} (*i.e.*, 40% of the total inflow) at the beginning of the procedure to 0 mL.min^{-1} after 16 min (*i.e.*, a 5 % decrease every 2 min).

A series of polystyrene sulfonate (PSS) reference standards (Polysciences, Eppelheim, Germany) of different molecular weights (0.891, 1.67, 3.42, 6.43, 15.8, 33.5 kDa; or respective size diameters 1.5, 2.0, 2.8, 3.8, 5.8, 8.2 nm see [60] for details) and a series of carboxylated polystyrene reference particles (Magsphere, USA) of different sizes (24, 60, 105, 207, and 420 nm) were used for size calibration. The calibration depends on various experimental conditions (membrane, eluent, flow rates, equipment, and operating time) and, thus, has to be checked carefully. Dispersions were freshly prepared in the carrier solution before injection. The PSS dispersions had a mass concentration of 100 µg.L^{-1} each, and the carboxylated polystyrene mass concentrations were 10, 5, 2, 2, and 10 mg.L^{-1} for the 24, 60, 105, 207, and 420 nm sizes, respectively. No overloading effect was observed by injection of 100 µL dispersion aliquots. At higher particle concentrations, electrostatic repulsion produces a continuous shift of the elution band to shorter elution times [61–63]. For the calibration of the AsFlFFF/ICP-MS arrangement, a solution containing the elements of interest in 6% nitric acid was prepared from ICP-MS standard solutions (Specpure (Alfa Aesar) and ICP Multi Element Standard Solution VI CertiPUR (Merck)). The methods for the conversion of raw ICP-MS fractogram data in counts per second (cps) into mass per second (ng.s^{-1}) and the quantification of sample component recoveries have been explained earlier [60].

2.3. Photon Correlation Spectroscopy

Complementary size informations are obtained by Photon Correlation Spectroscopy (PCS). The equipment is a homodyne single beam ZetaPlus System equipped with a 50 mW solid-state laser emitting at 632 nm (Brookhaven Inc, USA). For the PCS measurements, 3 mL of the supernatants obtained after centrifugation are placed in a disposable plastic cuvette and measured over two runs consisting of 10 measurements of 15 s each, *i.e.*, 20 measurements, for determination of mean hydrodynamic diameters. The corresponding volume-weighted diameter values (PCSv) are those which can be compared directly with the AsFlFFF data.

3. Results and Discussion

3.1. Preliminary Considerations: Distinguishing Adsorption from Incorporation of Pollutant on/in Nanoparticles from an AsFlFFF/ICP-MS Fractogram

Figure 1 shows examples for typical fractograms of a colloid sample with a multimodal size distribution and a main structural component A eluted either in normal mode (Figure 1-I) or in steric mode (Figure 1-II). Colloid elution according to the size is different in both modes. When assuming a trace component M being structurally incorporated in the particles, the ICP-MS signal ratio for both components A/M is expected to remain constant for all particle sizes, whatever the elution mode is. The recoveries for both components A and M are also expected to be similar. The situation is different if the trace component M is adsorbed on the colloid surface. The colloid associated amount of M should follow the surface area to volume ratio. As a consequence, the A/M ratio will increase continuously over the fractogram in the normal mode, whereas the ratio will decrease in the steric mode. Finally, the recoveries of A and M can be different if the sorption is fraction-dependent or if the desorption of M during fractionation depends on colloid size and residence time.

The situation might be more complex in reality, if e.g., the incorporation is size dependent, if both adsorbed and incorporated species coexist in a sample or if the elution mode is not entirely clear. Careful inspection and interpretation of the fractograms are then required.

3.2. Analysis of Hectorite Nanoparticles Synthesized in the Presence of La, Eu, Yb

3.2.1. Fractograms and Particle Size Distribution

Magnesium as a structural element of hectorite is used as an indicator for the dispersed NPs in suspension. Figure 2 presents the Mg-, La-, Eu-, and Yb-ICP-MS fractograms, representing the measured elemental mass as a function of the elution time for 3LnCopHec-sup. The laser light scattering (LLS) fractogram of the same sample (Figure 2) indicates an elution in normal mode as the intensity increases with the elution time. Fractograms were subsequently converted [59,60] into mass concentrations as a function of the hydrodynamic diameter according to the previously performed size calibration (Figure 3).
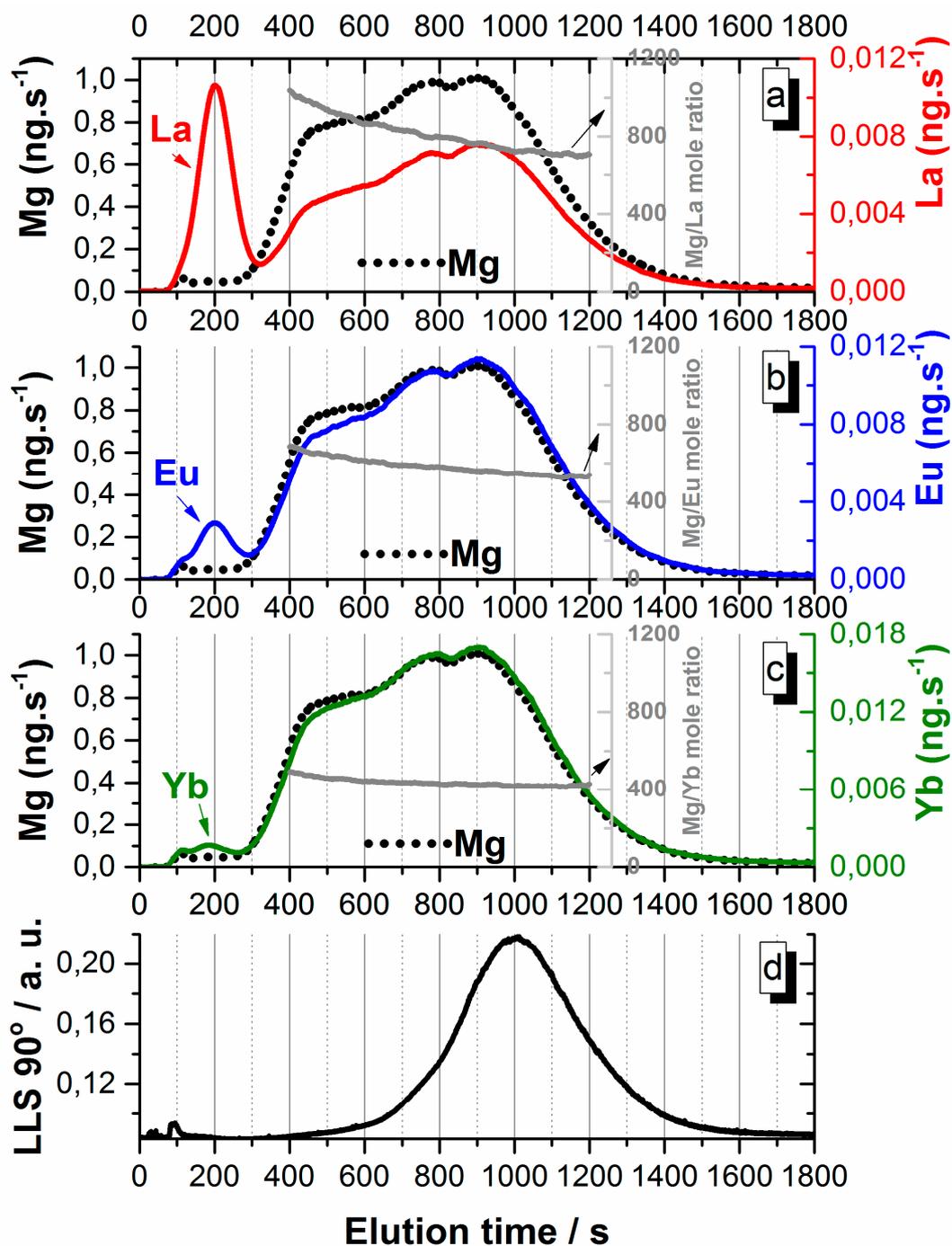
Figure 2. ICP-MS fractograms for Mg (black dots in a, b, and c), La (**a**), Eu (**b**), and Yb (**c**), and with laser light scattering (LLS) detection (**d**) obtained after injection of diluted 3LnCopHec-sup. Data obtained for injection of 100 µL, mean of two injections, smoothed data.
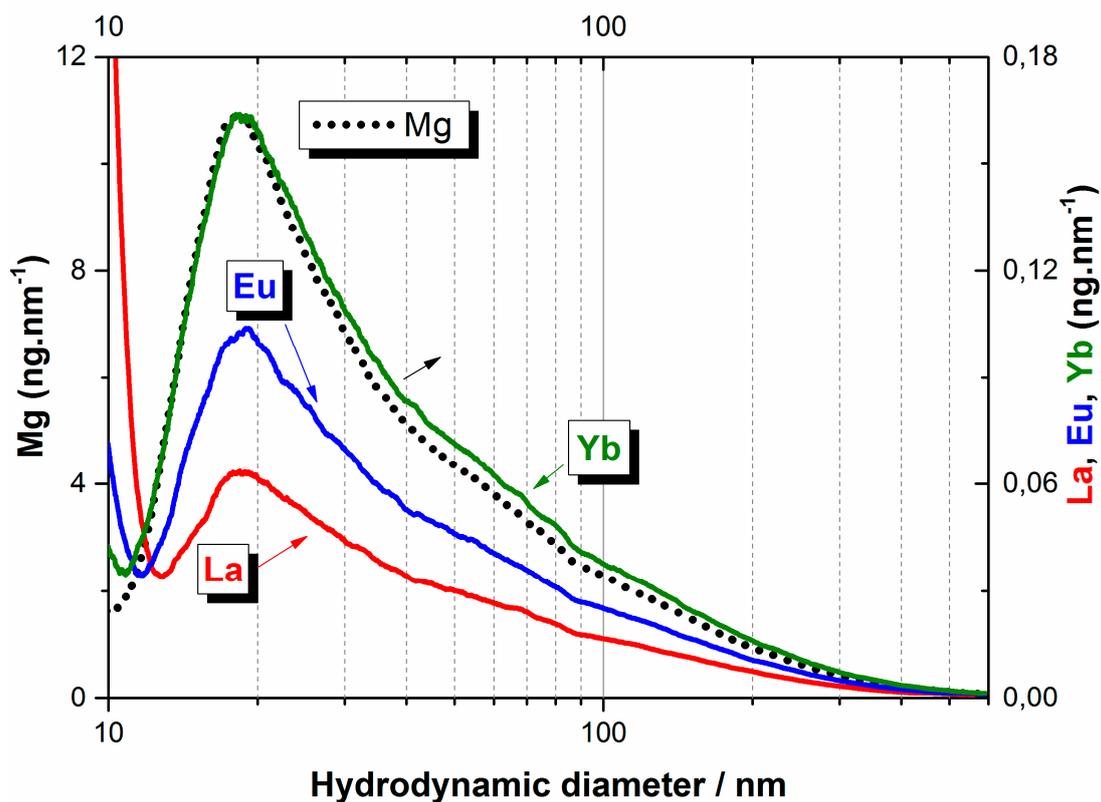
Figure 3. NPs size distribution determined from Mg (black dots), La (red line), Eu (blue line), and Yb (green line) obtained after conversion of the data from Figure 2.

The Mg fractogram of 3LnCopHec-sup (Figure 2) reveals the existence of NPs with a multimodal size distribution. These NPs remain thus dispersed after the centrifugation until the injection and measurement. No attempt was made to follow the evolution of the hectorite particles dispersed in the supernatant after this measurement. The first feature of the fractogram is located at t ~100 s (the void peak) and corresponds to non-retarded species. This peak has only low intensity and thus corresponds to a minor fraction of the sample. The signal recorded for longer elution times corresponds to hectorite particles. Their sizes range from 10 to 500 nm (Figure 3), with some peaks and shoulders clearly visible (Figure 2) at ~450 s (~19 nm), ~750 s (~64 nm), ~900 s (~123 nm) and ~1050 s (~239 nm). The mean value calculated from the AsFlFFF fractograms is (45 ± 3) nm. Multimodal size distributions have also been reported recently for NPs mobilized from bulk suspensions of hectorite synthesized under similar conditions in the presence of only Eu [13] or Lu [16]. In both studies, the elution occurred in normal mode and the eluted particles were of similar sizes, ranging from ~10 to 300 nm. The fractograms also had clear peaks and shoulders at ~22, 110, and 156 nm in the Lu study and at ~15, 70, 105, and 140 nm in the Eu study. Additionally, the smallest particles in 3LnCopHec-sup (~19 nm), in ColEuCopHec (~17 nm, [13]) and in ColLuCopHec (~22 nm, [16]) have similar sizes, close to the reported value (19.5 nm) obtained by line-shape analysis (XRD) for synthetic Li-hectorite (*i.e.*, hectorite without interacted lanthanide) [11]. The corresponding mean volume-weighted diameter values (PCSv) is ~51 nm with particles detected in the size range varying from 25 nm to 260 nm. PCS and AsFlFFF data are thus consistent. These values are also consistent with small-angle neutron scattering (SANS) studies giving 33 nm as an average thickness of the clay stack of synthetic Li-hectorite particles [57]. Note that size information obtained

by AsFlFFF, giving a mean equivalent sphere diameter of the particle, is different from that obtained by XRD or SANS which provide information on the coherent scattering domain size (*i.e.*, crystallite size in the direction perpendicular to the lattice plane) and on the thickness of the lamella, respectively. Sizes differing by a factor of 2 may thus be considered more or less identical. In conclusion, this finding indicates that the presence of a single, or several, lanthanide(s) during the hectorite synthesis does not affect the size of the nanoparticles that can be mobilized from the bulk.

3.2.2. Lanthanides Interaction with Hectorite in 3LnCopHec-sup

The Mg content in the NPs of sizes <10 nm (<300 s) is relatively low, while the contribution of the lanthanides increases significantly from Yb to La (Figure 2). Apparently a size-dependent association of the lanthanides to the hectorite takes place, excluding the larger sized Lns to form separate colloidal phases. The Ln exclusion does not take place during the first step of the hectorite synthesis, where the Ln(III) are completely incorporated into the brucite precursors [8]. As a consequence, larger sized cations are released during the clay crystallization after addition of silica and the formation of tetrahedral octahedral tetrahedral (TOT) layers. Such behavior may be explained by the incompatibility of the larger sized Ln(III) ions with the hectorite structure. Obviously Mg(II) replacement by larger- sized Ln(III) ions in the clay octahedral site induces excessive structural strain leading to expulsion and either Ln(III) adsorption on hectorite surfaces or formation of some kind of mixed silica colloids, as Si is present in excess. The peak at ~10 nm (~200 s) can thus be assigned to Ln(III) containing silica NP.

For larger-sized particles in the size range 15–500 nm the ICP-MS-fractograms of the lanthanides (La, Eu, Yb) are correlated with each other and with the Mg pattern (Figures 2 and 3). The position of the maxima is the same and the shape of the Mg and Yb fractograms are almost identical. For Eu, a deviation becomes apparent in the sense that the relative association to smaller NP sizes decreases, which is even more pronounced for La. In addition, a significantly lower element recovery during fractionation is found for La as compared to Mg, Yb and Eu (Table 2). The Mg, Eu, and Yb recoveries are very similar to reported values [13,16]. Exact reasons for the only moderate recovery of Mg after fractionation in the channel are not presently known. Respective values are, however, very reproducible from one injection to another and very similar from one study to the other.

The variation of Ln elution pattern becomes apparent on the fractograms by looking at the Mg/M^{n+} molar ratios (M^{n+}: La, Eu or Yb) over the full size range. This ratio is almost constant for Yb, but decreases for increasing NPs sizes for Eu, and even more for La. The mean values of the molar ratio are reported Table 2: measured in the bulk suspension (named "bulk hectorite") or in the NPs distribution (named "NPs").

For the smallest lanthanide Yb, the Mg:Yb molar ratio in the bulk hectorite is similar to that in the NPs of hectorite (Table 2). This reflects that Yb is almost entirely colloidal and, thus, associated with the hectorite NPs. In addition the ratio is quasi-constant, which suggests a homogeneous incorporation into the NP via a random substitution for Mg. This result agrees with data obtained for Lu-hectorite interaction studies as Yb has almost the same ionic radius [15] as Lu ($r(^{VI}(Lu(III)) = 0.86$ Å, $r(^{VI}Yb(III)) = 0.87$ Å). The mean Mg:Eu molar ratio value (slightly lower in the bulk compared to the NPs, Table 2) might reflect a loss of element in agreement with the slight decrease in Mg/Eu molar ratio observed in the

fractogram for increasing size. This agrees with earlier studies [13] and indicates as well the incorporation in hectorite, though with a slight preference to larger particles not seen for Yb.

Table 2. Elemental recoveries and Mg/M^{n+} molar ratio for the different dispersions (M^{n+}: La, Eu, Yb, Zr, Th), bulk: as determined from direct ICP-MS measurements; NPs: as determined from the fractogram analysis.

3LnCopHec-sup				
	Mg	**La**	**Eu**	**Yb**
Recovery (%) <300 s	0.40 ± 0.05	7.9 ± 0.1	2.0 ± 0.1	3.8 ± 0.1
Recovery (%) 300–1800 s	59 ± 4	45 ± 4	58 ± 4	63 ± 4
Mg/M^{n+} Molar ratios Bulk hectorite NPs: 400–1200 s	-	580 ± 40 814 ± 90	556 ± 38 584 ± 42	454 ± 30 436 ± 19

3LnZrCopHec-sup					
	Mg	**La**	**Eu**	**Yb**	**Zr**
Recovery (%) <200 s	0.28 ± 0.05	1.62 ± 0.02	0.89 ± 0.03	$0.48 \pm 0\ 03$	4.9 ± 0.2
Recovery (%) 200–1800 s	59 ± 2	63 ± 2	64 ± 2	65 ± 3	61 ± 1
Mg : M^{n+} Molar ratios Bulk hectorite NPs: 300–1100 s		584 ± 60 580 ± 38	323 ± 34 307 ± 13	233 ± 30 215 ± 5	263 ± 20 382 ± 38

3LnThCopHec-sup					
	Mg	**La**	**Eu**	**Yb**	**Th**
Recovery (%) <300 s	0.03 ± 0.06	0.9 ± 0.1	0.69 ± 0.01	0.48 ± 0.03	1.6 ± 0.2
Recovery (%) 300–1800 s	64 ± 2	64 ± 2	68 ± 2	69 ± 2	66 ± 3
Mg : M^{n+} Molar ratios Bulk hectorite NPs:400–1200 s	-	668 ± 20 688 ± 48	618 ± 17 591 ± 35	552 ± 15 518 ± 17	624 ± 18 622 ± 60

The clear difference in the Mg:La molar ratios between the bulk and the NPs of hectorite indicates clearly that part of La is not associated with the colloidal hectorite NPs. This agrees with the La fractogram presented Figure 2 showing the elution of a separate La colloidal phase. Furthermore, a significant enrichment into hectorite NP of larger size is found for La, discernable by the pronounced Mg/La molar ratio decrease with elution time. This definitely does not indicate an adsorption process, which would result in the opposite trend (see Figure 1). The experimental finding is currently explained

by a preferential incorporation into larger brucite precursor particles during clay crystallization. Larger-sized brucite particles may provide a better compensation of strain and distortion induced by La substitution for Mg in octahedral edge sites. Smaller brucite particles cannot compensate the distortion or less easily. Additionally, as La is expected to be randomly distributed in brucite, fewer La atoms are expected to be located close to the brucite particle edges with increasing particle sizes. When located close to the particles edges, La ions may be expelled easier from the mineral than in the case of La ions positioned in the inner part of the crystal lattice. Additionally, structural distortion may be higher at the particle edges as compared to the center and, thus, the La release would be favored when located at distorted octahedral edge sites. This reasoning may explain the lower La content in the smaller particles. Because the structure is less distorted for incorporated Eu or Yb with smaller ionic radii, the release is far lower for these smaller cations. Finally, the elemental recoveries and the size dependent Mg/M^{n+} ratio pattern both clearly indicate a dependence of Ln incorporation on ionic radius.

This finding made for NP synthesized in the laboratory is consistent with the shape of well-known lanthanide pattern found in natural sedimentary clay minerals. They also contain trace amounts of lanthanides and their abundance usually decreases with increasing ionic radius [54–56]. Adding Ln ions separately or in a mixture apparently neither changes recovery nor Mg/M^{n+} ratio pattern, at least for Yb and Eu. Under the experimental conditions applied in the present work, Ln ions are quite diluted and incorporated in a highly dispersed way. Thus, Ln-Ln interaction effects apparently do not play a significant role as already observed in XAS studies [12].

3.3. Analysis of Hectorite Nanoparticles Synthesized in the Presence of La, Eu, Yb and Zr or Th

3.3.1. Fractograms and Particle Size Distributions

Figure 4 presents the Mg-, La-, Eu-, Yb-, and Zr-ICP-MS fractograms, representing the measured elemental mass as a function of the elution time, after injection of 3LnZrCopHec-sup. The ICP-MS fractograms of Mg, La, Eu, Yb, and Th obtained after injection of the suspension 3LnThCopHec-sup are presented in Figure 5. The Mg-fractograms show that hectorite NPs are present in the two suspensions. Figures 4 and 5 contain also the LLS fractograms but compared to Figure 2, they show that the signal is high at the beginning of the elution fractogram which indicates the presence of large particles. The results obtained for the same supernatants injected following an on-line filtration at 450 nm confirm this statement. Less than 7% of Mg is recovered for 3LnZrCopHec-sup and even less (<3%) for 3LnThCopHec-sup in the size range 600–1500 s. In agreement, PCS data indicate the presence of broad size distribution in the range 50 nm up to 1.5 μm for the unfiltered dispersion. One can thus conclude that the elution occurs at least partly in steric mode after injection of those two supernatants. The corresponding fractograms are consequently only presented in measured mass as a function of the elution time and are not converted in mass as a function of the hydrodynamic diameter.
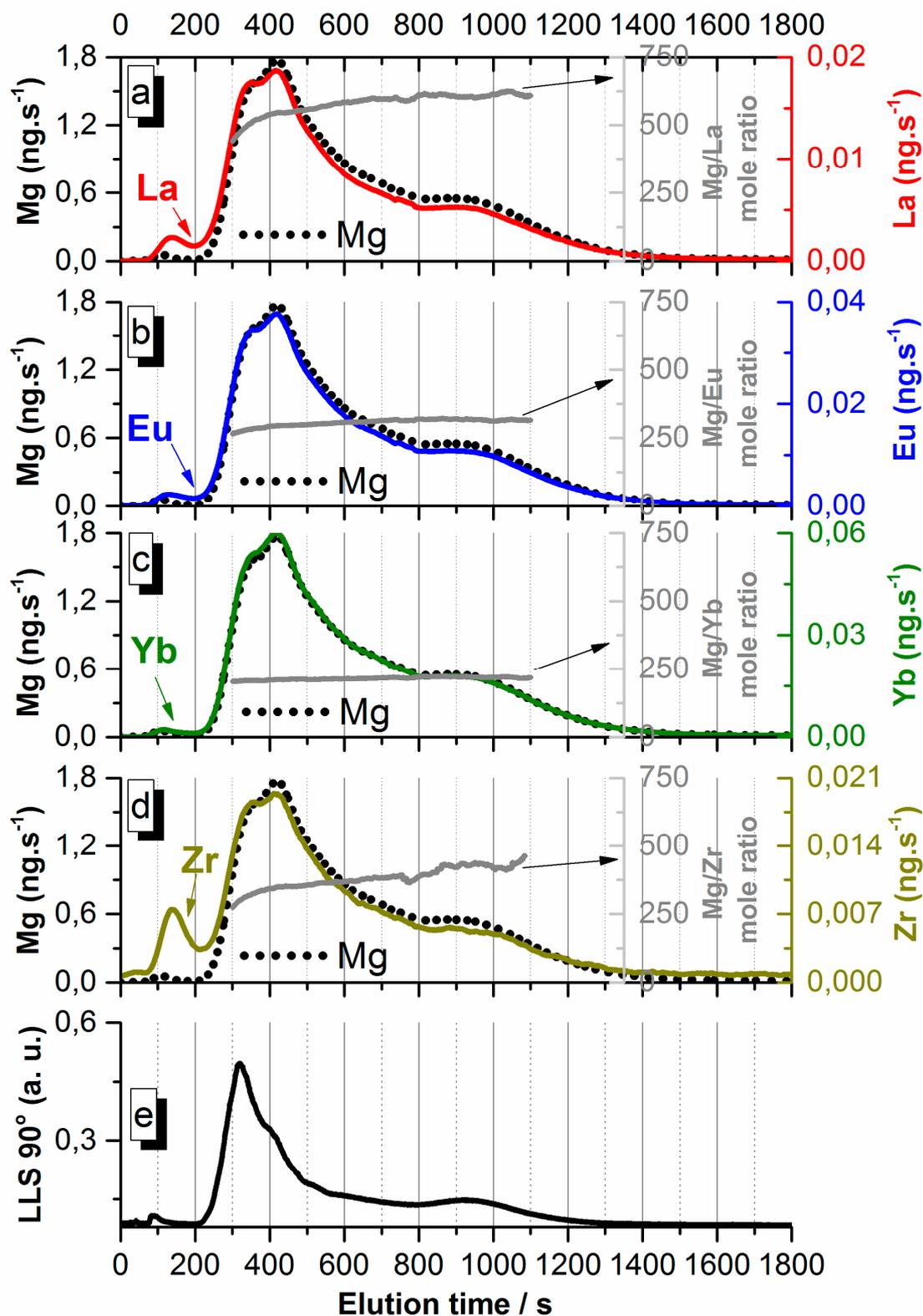
Figure 4. ICP-MS fractograms, in mass per time, of Mg (black dots in **a**, **b**, **c**, and **d**), La (**a**), Eu (**b**), Yb (**c**), Zr (**d**), and laser light scattering (LLS) fractogram (**e**) obtained after injection of diluted 3LnZrCopHec-sup. Data obtained for injection of 100 μL, mean of two injections, smoothed data.
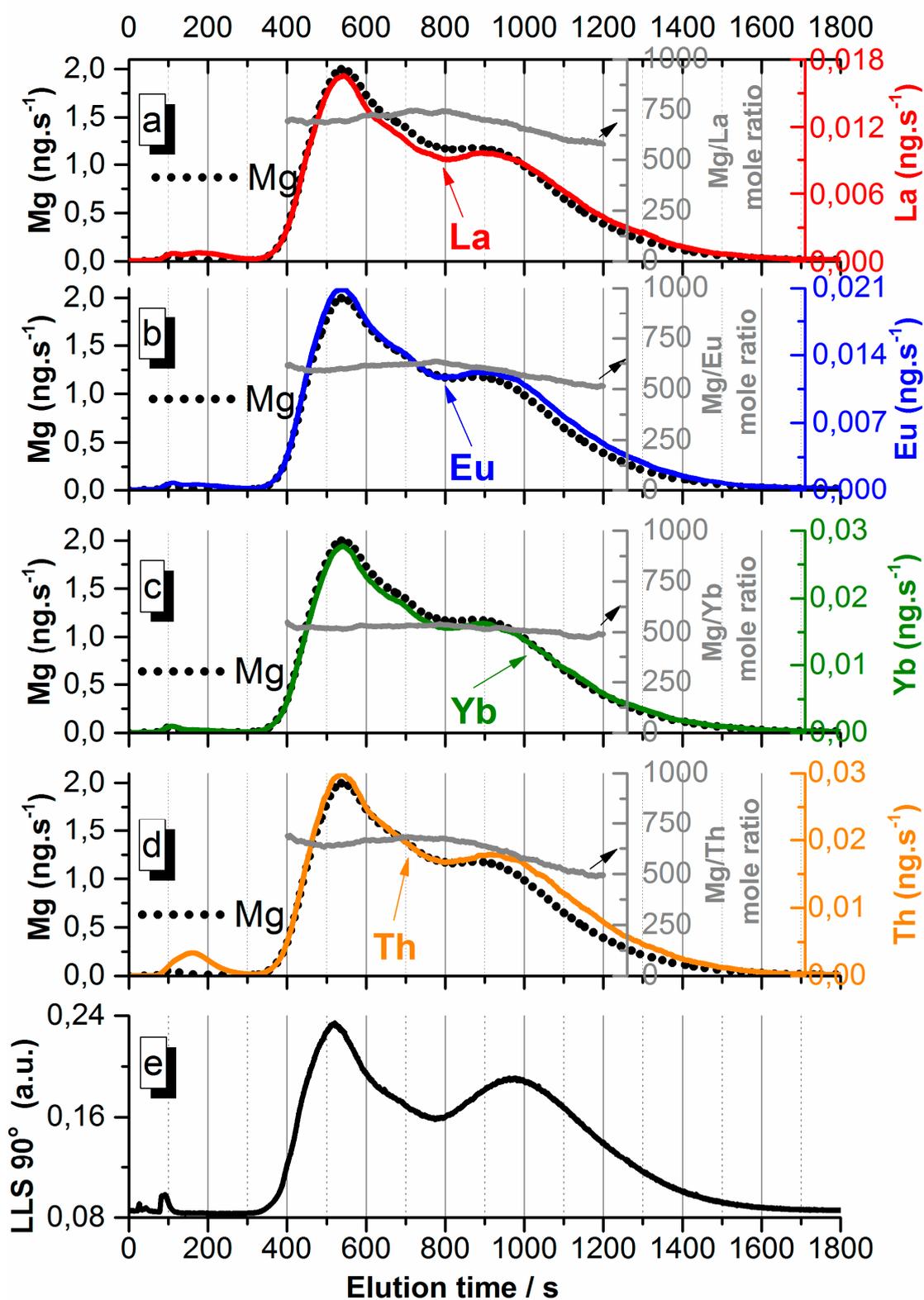
Figure 5. ICP-MS fractograms, in mass per time, of Mg (black dots in **a**, **b**, **c**, and **d**), La (**a**), Eu (**b**), Yb (**c**), Th (**d**), and laser light scattering (LLS) fractogram (**e**) obtained after injection of diluted 3LnThCopHec-sup. Data obtained for injection of 100 µL, mean of two injections, smoothed data.

The particle size distributions of the suspensions 3LnZrCopHec-sup and 3LnThCopHec-sup appear broader compared to the suspension 3LnCopHec-sup. The presence of trace amounts of tetravalent Zr or Th can hardly explain the difference. A reason might be the significant difference in chemical conditions during the brucite precursor synthesis and, notably, the resulting ionic strength in the final suspension. In the original 3LnCopHec suspension, the base used to precipitate brucite was 2 M NH_4OH. For the suspensions with tetravalent element, the brucite was precipitated by addition of 10 M NaOH to a solution of either 0.93 M HCl (Th stock solution) or 1 M HCl (Zr stock solution). The final pH achieved by using NH_4OH was ~9.5 and by using NaOH, it was ~11. Literature data [64,65] show clearly that differences in temperature, pH of the suspensions or nature of the base counter-ions drastically affect the brucite crystals growth. Accordingly, using 10 M NaOH instead of 2 M NH_4OH as used previously might be considered as the main parameter influencing the nucleation rate and thus the polydispersity of the brucite particles formed. Consequently, the resulting TOT assemblages of hectorite clay particles which have a similar width and length as their brucite precursors are of larger sizes.

3.3.2. Lanthanides and Tetravalent Elements Interaction with Hectorite in 3LnZrCopHec-sup and 3LnThCopHec-sup

For the suspensions 3LnZrCopHec-sup and 3LnThCopHec-sup, except for Zr, the similarities between the "bulk hectorite" and the "NPs" molar ratios (Table 2) reflect that the elements are bound to the hectorite NPs. A part of the Zr may also form a separate (colloidal) phase.

In general, on the fractograms, a similar elution pattern is observed for all the elements, pointing to an at least partial incorporation into hectorite particles. Nevertheless, the Zr- and Th-fractogram pattern reveal a higher variability as compared to those of Yb or Eu and are similar to those found for La. Similar conclusions as have been drawn for hectorite NPs containing only lanthanides can thus been drawn.

For the smallest lanthanide (Yb) the Mg:Yb molar ratio again is constant over the entire size range for both supernatants (Figures 4 and 5, and Table 2) indicating a very homogeneous incorporation into all hectorite size fractions, which apparently is not affected by the presence of Zr or Th.

Molar ratios for Eu, La, Zr (Figure 4) or Th (Figure 5) related to Mg show a clear dependence on the elution time. Assuming a predominant elution in steric mode for the Zr-containing sample, the slight increase of the $Mg:M^{n+}$ ratio might be interpreted as a slight depletion in elements for decreasing hectorite particle sizes (Figure 1). This is consistent with our previous observations (Figure 2) in absence of tetravalent element. For the Th-containing sample, such a clear relationship is not observed. We assume that, due to the wide particle size range, the elution mode consists of a complex superposition of steric and normal size fractionation.

Interestingly, the higher La recoveries (63% ± 2% and 64% ± 2%) recorded for 3LnZrCopHec-sup and 3LnThCopHec-sup, respectively, might be related to the presence of larger-sized particles than found in the 3LnCopHec-sup sample. This is a further indication that the larger the particle size, the better the tolerance of the hectorite crystals for larger cation incorporation. The Zr(IV) ionic radius is similar to that of Mg ($r(^{VI}Zr(IV)) = 0.72$ Å, $r(^{VI}Mg(II)) = 0.72$ Å) and, thus, should show a better compatibility with the hectorite structure than found for e.g., Th and La. However, the charge is double than that of Mg(II) and, thus, requires significant charge compensation. Hydrolysis and formation of Zr oxihydroxide colloids may, furthermore, act as a competing reaction during hectorite synthesis [66,67].

Such small Zr oxihydroxide colloids might be visible in the early elution part of the fractogram (between 100 and 300 s) and explain the difference between the bulk and the NPs molar ratios

For the somewhat larger-sized Th(IV) ion ($r(^{VI}(Th(IV)) = 0.94$ Å), basically the same observations are made as for Zr(IV). In conclusion, the data show that both Th and Zr can substitute for some Mg in the brucite precursors. Nevertheless, the elution in mixed modes heavily complicates the interpretation of the data. To allow for a better and straightforward interpretation, different separation program would have been necessary.

4. Conclusions

Hectorite was synthesized in the simultaneous presence of several lanthanides and tetravalent cations following a multi-step synthesis protocol. The smallest particles were isolated by centrifugation and analyzed by AsFlFFF/ICP-MS to gain insight into the elemental content as a function of the particle size. The comparison of molar ratios for Mg and those of the co-precipitated trivalent and tetravalent elements is taken to discuss possible incorporation reactions.

The synthesis of hectorite NPs in the presence of a mixture of several lanthanide ions does not show different results as compared to synthesis in the presence of a single Ln ion. AsFlFFF/ICP-MS results show significant differences neither in the extent nor in the size-dependent incorporation. Apparently, the ionic radius of the Ln ion determines the extent of incorporation in agreement with general considerations that larger-sized ions are less easily accommodated by the hectorite crystal lattice. Strain and structural distortion appear to be less pronounced for larger particles. The data show, for the first time, that some tetravalent elements, Zr(IV) and Th(IV), can be incorporated into hectorite nanoparticles, at least at trace concentrations.

Under particular conditions, radionuclides may be incorporated into nano-sized hectorite or other clay-like secondary phases forming during corrosion of vitrified HLW. Accordingly, the hectorite NPs might be considered as simulates for radionuclide-bearing NPs which can be generated in a deep geological repository. Inflow of, e.g., low ionic strength groundwater can, in principle, mobilize such particles, which then might act as RNs carriers if and only if they are stable under the specific (geo)chemical conditions and if the structural retention is not reversible. This still needs to be demonstrated. It is clear that under the given conditions of corroding borosilicate glass in a repository, kinetics and geochemical parameters will be clearly different from the synthesis conditions in the present study. Nevertheless, our results can be considered as a proof of principle that incorporation of lanthanides/actinides into hectorite NPs is possible.

Author Contributions

Muriel Bouby and Nicolas Finck conceived and designed the experiments; Nicolas Finck performed all the hectorite syntheses; Muriel Bouby performed the measurements and data treatment; Muriel Bouby, Nicolas Finck and Horst Geckeis analyzed the data and wrote the paper.

Conflicts of Interest

The authors declare no conflict of interest.

Appendix
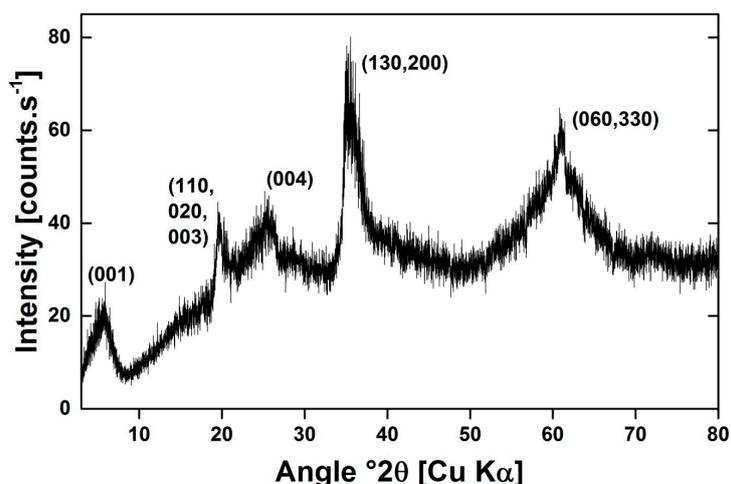
Figure A1. X-ray diffractogram of the hectorite synthesized in the presence of La, Eu, Yb, and Th. The number in parentheses indicate the lattice planes. Only smectite could be detected on the diffractogram, no other (crystalline) phase could be evidenced, *i.e.*, no brucite precursor phase was detected. The presence of trace amounts of dopants thus did not affect the smectite synthesis procedure.

References

1. Donald, I.W. *Waste Immobilization in Glass and Ceramic Based Hosts: Radioactive Toxic and Hazardous Wastes*; John Wiley and Sons, Ltd.: Chichester, West Sussex, UK, 2010.
2. Thien, B.; Godon, N.; Hubert, F.; Angéli, F.; Gin, S.; Ayral, A. Structural identification of a trioctahedral smectite formed by the aqueous alteration of a nuclear glass. *Appl. Clay Sci.* **2010**, *49*, 135–141.
3. Debure, M.; Frugier, P.; De Windt, L.; Gin, S. Borosilicate glass alteration driven by magnesium carbonates. *J. Nucl. Mater.* **2012**, *420*, 347–361.
4. Buck, E.C.; Bates, J.K. Microanalysis of colloids and suspended particles from nuclear waste glass alteration. *Appl. Geochem.* **1999**, *14*, 635–653.
5. Ledergerber, G.; Herbst, R.; Zwicky, H.U.; Kutter, H.; Fischer, P. Characterization and quality control of uranium-plutonium carbide for the AC-3/FFTF experiment. *J. Nucl. Mater.* **1988**, *153*, 189–204.

6. Jollivet, P.; Gin, S.; Schumacher, S. Forward dissolution rate of silicate glasses of nuclear interest in clay-equilibrated groundwater. *Chem. Geol.* **2012**, *330–331*, 207–217.

7. Jollivet, P.; Frugier, P.; Parisot, G.; Mestre, J.P.; Brackx, E.; Gin, S.; Schumacher, S. Effect of clayey groundwater on the dissolution rate of the simulated nuclear waste glass SON68. *J. Nucl. Mater.* **2012**, *420*, 508–518.

8. Brandt, H.; Bosbach, D.; Panak, P.J.; Fanghänel, T. Structural incorporation of Cm(III) in trioctahedral smectite hectorite: A time-resolved laser fluorescence spectroscopy (TRLFS) study. *Geochim. Cosmochim. Acta* **2007**, *71*, 145–154.

9. Pieper, H.; Bosbach, D.; Panak, P.J.; Rabung, T.; Fanghänel, T. Eu(III) coprecipitation with the trioctahedral clay mineral, hectorite. *Clays Clays Miner.* **2006** *54*, 45–53.

10. Finck, N.; Stumpf, T.; Walther, C.; Bosbach, D. TRLFS characterization of Eu(III)-doped synthetic organo-hectorite. *J. Contamin. Hydrol.* **2008**, *102*, 253–262.

11. Carrado, K.A.; Thiyagarajan, P.; Song, K. A study of organo-hectorite clay crystallization. *Clay Miner.* **1997**, *32*, 29–40.

12. Finck, N.; Schlegel, M.L.; Bosbach, D. Sites of Lu(III) sorbed to and coprecipitated with hectorite. *Environ. Sci. Technol.* **2009**, *43*, 8807–8812.

13. Finck, N.; Bouby, M.; Dardenne, K.; Geckeis, H. Characterization of Eu(III) co-precipitated with and adsorbed on hectorite: From macroscopic crystallites to nanoparticles. *Mineral. Magaz.* **2012**, *76*, 2723–2740.

14. Finck, N.; Dardenne, K.; Geckeis, H. Am(III) coprecipitation with and adsorption on the smectite hectorite. *Chem. Geol.* **2015**, *409*, 12–19.

15. Shannon, R.D. Revised effective ionic radii and systematic studies of interatomic distances in halides and chalcogenides. *Acta Crystallogr.* **1976**, *A32*, 751–767.

16. Bouby, M.; Finck, N.; Geckeis, H. Flow field-flow fractionation (FlFFF) coupled to sensitive detection techniques: A way to examine radionuclide interactions with nanoparticles. *Mineral. Magaz.* **2012**, *76*, 2709–2721.

17. Taylor, H.E.; Garbarino, J.R.; Murphy, D.M.; Beckett, R. Inductively coupled plasma-mass spectrometry as an element-specific detector for field-flow fractionation particle separation. *Anal. Chem.* **1992**, *64*, 2036–2041.

18. Dubascoux, S.; Le Hécho, I.; Hassellöv, M.; Von Der Kammer, F.; Potin Gautier, M.; Lespes, G. Field-flow fractionation and inductively coupled plasma mass spectrometer coupling: History, development and applications. *J. Anal. Atom. Spectrom.* **2010**, *25*, 613–623.

19. Wahlund, K.-G. Flow field-flow fractionation: Critical overview. *J. Chromatogr. A* **2013**, *1287*, 97–112.

20. Gigault, J.; Pettibone, J.M.; Schmitt, C.; Hackley, V.A. Rational strategy for characterization of nanoscale particles by asymmetric-flow field flow fractionation: A tutorial. *Anal. Chim. Acta* **2014**, *809*, 9–24.

21. Herrero, P.; Bäuerlein, P.S.; Emke, E.; Pocurull, E.; de Voogt, P. Asymmetrical flow field-flow fractionation hyphenated to Orbitrap high resolution mass spectrometry for the determination of (functionalised) aqueous fullerene aggregates. *J. Chromatogr. A* **2014**, *1356*, 277–282.

22. Pornwilard, M.-M.; Siripinyanond, A. Field-flow fractionation with inductively coupled plasma mass spectrometry: Past, present, and future. *J. Anal. Atom. Spectrom.* **2014**, *29*, 1739–1752.

23. Lapresta-Fernández, A.; Salinas-Castillo, A.; Anderson De La Llana, S.; Costa-Fernández, J.M.; Domínguez-Meister, S.; Cecchini, R.; Capitán-Vallvey, L.F.; Moreno-Bondi, M.C.; Marco, M.-P.; Sánchez-López, J.C.; *et al.* A general perspective of the characterization and quantification of nanoparticles: Imaging, spectroscopic, and separation techniques. *Crit. Rev. Solid State Mater. Sci.* **2014**, *39*, 423–458.

24. Hell, J.; Kneifel, W.; Rosenau, T.; Böhmdorfer, S. Analytical techniques for the elucidation of wheat bran constituents and their structural features with emphasis on dietary fiber—A review. *Trends Food Sci. Technol.* **2014**, 35, 102–113.

25. Yohannes, G.; Jussila, M.; Hartonen, K.; Riekkola, M.-L. Asymmetrical flow field-flow fractionation technique for separation and characterization of biopolymers and bioparticles. *J. Chromatogr. A* **2011**, *1218*, 4104–4116.

26. Qureshi, R.N.; Kok, W.T. Application of flow field-flow fractionation for the characterization of macromolecules of biological interest: A review. *Anal. Bioanal. Chem.* **2011**, *399*, 1401–1411.

27. Rambaldi, D.C.; Reschiglian, P.; Zattoni, A. Flow field-flow fractionation: Recent trends in protein analysis. *Anal. Bioanal. Chem.* 2011, *399*, 1439–1447.

28. Horie, M.; Kato, H.; Iwahashi, H. Cellular effects of manufactured nanoparticles: Effect of adsorption ability of nanoparticles. *Arch. Toxicol.* **2013**, *87*, 771–781.

29. Zattoni, A.; Roda, B.; Borghi, F.; Marassi, V.; Reschiglian, P. Flow field-flow fractionation for the analysis of nanoparticles used in drug delivery. *J. Pharm. Biomed. Anal.* **2014**, *87*, 53–61.

30. Wagner, M.; Holzschuh, S.; Traeger, A.; Fahr, A.; Schubert, U.S. Asymmetric flow field-flow fractionation in the field of nanomedicine. *Anal. Chem.* **2014**, *86*, 5201–5210.

31. Thang, N.M.; Knopp, R.; Geckeis, H.; Kim, J.I.; Beck, H.P. Detection of nanocolloids with flow-field flow fractionation and laser- induced breakdown detection. *Anal. Chem.* **2000**, *72*, 1–5.

32. Geckeis, H.; Ngo Manh, T.; Bouby, M.; Kim, J.I. Aquatic colloids relevant to radionuclide migration: Characterization by size fractionation and ICP-mass spectrometric detection. *Colloid. Surf. A* **2003**, *217*, 101–108.

33. Bouby, M.; Geckeis, H.; Ngo Manh, T.; Yun, J.-I.; Dardenne, K.; Schäfer, T.; Walther, C.; Kim, J.-I. Laser-induced breakdown detection combined with asymmetrical flow field-flow fractionation: Application to iron oxi/hydroxide colloid characterization. *J. Chromatogr. A* **2004**, *1040*, 97–104.

34. Schäfer, T.; Geckeis, H.; Bouby, M.; Fanghänel, T. U, Th, Eu and colloid mobility in a granite fracture under near-natural flow conditions. *Radiochim. Acta* **2004**, *92*, 731–737.

35. Suteerapataranon, S.; Bouby, M.; Geckeis, H.; Fanghänel, T.; Grudpan, K. Interaction of trace elements in acid mine drainage solution with humic acid. *Water Res.* **2006**, *40*, 2044–2054.

36. Domingos, R.F.; Baalousha, M.A.; Ju-Nam, Y.; Reid, M.M.; Tufenkji, N.; Lead, J.R.; Leppard, G.G.; Wilkinson, K.J. Characterizing manufactured nanoparticles in the environment: Multimethod determination of particle sizes. *Environ. Sci. Technol.* **2009**, *43*, 7277–7284.

37. Hassellöv, M.; Kaegi, R. Analysis and Characterization of Manufactured Nanoparticles in Aquatic Environments. *Environ. Human Health Imp. Nanotechnol.* **2009**, 211–266.

38. Baalousha, M.; Stolpe, B.; Lead, J.R. Flow field-flow fractionation for the analysis and characterization of natural colloids and manufactured nanoparticles in environmental systems: A critical review. *J. Chromatogr. A* **2011**, *1218*, 4078–4103.

39. Bouby, M.; Geckeis, H.; Lützenkirchen, J.; Mihai, S.; Schäfer, T. Interaction of bentonite colloids with Cs, Eu, Th and U in presence of humic acid: A flow field-flow fractionation study. *Geochim. Cosmochim. Acta* **2011**, *75*, 3866–3880.

40. Jiménez, M.S.; Gómez, M.T.; Bolea, E.; Laborda, F.; Castillo, J. An approach to the natural and engineered nanoparticles analysis in the environment by inductively coupled plasma mass spectrometry. *Int. J. Mass Spectrom.* **2011**, *307*, 99–104.

41. Kammer, F.V.D.; Legros, S.; Hofmann, T.; Larsen, E.H.; Loeschner, K. Separation and characterization of nanoparticles in complex food and environmental samples by field-flow fractionation. *TrAC - Trends Anal. Chem.* **2011**, *30*, 425–436.

42. Rezić, I. Determination of engineered nanoparticles on textiles and in textile wastewaters. *TrAC - Trends Anal. Chem.* **2011**, *30*, 1159–1167.

43. Silva, B.F.D.; Pérez, S.; Gardinalli, P.; Singhal, R.K.; Mozeto, A.A.; Barceló, D. Analytical chemistry of metallic nanoparticles in natural environments. *TrAC - Trends Anal. Chem.* **2011**, *30*, 528–540.

44. Ulrich, A.; Losert, S.; Bendixen, N.; Al-Kattan, A.; Hagendorfer, H.; Nowack, B.; Adlhart, C.; Ebert, J.; Lattuada, M.; Hungerbühler, K. Critical aspects of sample handling for direct nanoparticle analysis and analytical challenges using asymmetric field flow fractionation in a multi-detector approach. *J. Anal. Atom. Spectrom.* **2012**, *27*, 1120–1130.

45. Bandyopadhyay, S.; Peralta-Videa, J.R.; Gardea-Torresdey, J.L. Advanced analytical techniques for the measurement of nanomaterials in food and agricultural samples: A review. *Environ. Eng. Sci.* **2013**, *30*, 118–125.

46. Lapworth, D.J.; Stolpe, B.; Williams, P.J.; Gooddy, D.C.; Lead, J.R. Characterization of suboxic groundwater colloids using a multi-method approach. *Environ. Sci. Technol.* **2013**, *47*, 2554–2561.

47. Plathe, K.L.; von der Kammer, F.; Hassellöv, M.; Moore, J.N.; Murayama, M.; Hofmann, T.; Hochella, M.F. The role of nanominerals and mineral nanoparticles in the transport of toxic trace metals: Field-flow fractionation and analytical TEM analyses after nanoparticle isolation and density separation. *Geochim. Cosmochim. Acta* **2013**, *102*, 213–225.

48. Stolpe, B.; Guo, L.; Shiller, A.M. Binding and transport of rare earth elements by organic and iron-rich nanocolloids in alaskan rivers, as revealed by field-flow fractionation and ICP-MS. *Geochim. Cosmochim. Acta* **2013**, *106*, 446–462.

49. Bolea, E.; Jiménez-Lamana, J.; Laborda, F.; Abad-Álvaro, I.; Bladé, C.; Arola, L.; Castillo, J.R. Detection and characterization of silver nanoparticles and dissolved species of silver in culture medium and cells by AsFlFFF-UV-Vis-ICPMS: Application to nanotoxicity tests. *Analyst* **2014**, *139*, 914–922.

50. Gottselig, N.; Bol, R.; Nischwitz, V.; Vereecken, H.; Amelung, W.; Klumpp, E. Distribution of phosphorus- containing fine colloids and nanoparticles in stream water of a forest catchment. *Vadose Zone J.* **2014**, *13*, 1539–1663.

51. Regelink, I.C.; Voegelin, A.; Weng, L.; Koopmans, G.F.; Comans, R.N.J. Characterization of colloidal Fe from soils using field-flow fractionation and Fe K-edge X-ray absorption spectroscopy. *Environ. Sci. Technol.* **2014**, *48*, 4307–4316.

52. Stolpe, B.; Zhou, Z.; Guo, L.; Shiller, A.M. Colloidal size distribution of humic- and protein-like fluorescent organic matter in the northern Gulf of Mexico. *Marine Chem.* **2014**, *164*, 25–37.

53. Huber, F.M.; Heck, S.; Truche, L.; Bouby, M.; Brendlé, J.; Hoess, P.; Schäfer, T. Radionuclide desorption kinetics on synthetic Zn/Ni-labeled montmorillonite nanoparticles. *Geochim. Cosmochim. Acta* **2015**, *148*, 426–441.

54. Severmann, S.; Mills, R.A.; Palmer, M.R.; Fallick, A.E. The origin of clay minerals in active and relict hydrothermal deposits. *Geochim. Cosmochim. Acta* **2004**, *68*, 73–88.

55. Uysal, I.T.; Golding, S.D. Rare earth element fractionation in authigenic illite-smectite from late Permian clastic rocks, Bowen basin, Australia: Implications for physic-chemical environments of fluids during illitization. *Chem. Geol.* **2003**, *193*, 167–179.

56. Piper, D.Z. Rare earth elements in the sedimentary cycle: A summary. *Chem. Geol.* **1974**, *14*, 285–304.

57. Carrado, K.A.; Xu, L.; Gregory, D.M.; Song, K.; Seifert, S.; Botto, R.E. Crystallization of a layered silicate clay as monitored by small-angle X-ray scattering and NMR. *Chem. Mater.* **2000**, *12*, 3052–3059.

58. Giddings, J.C.; Yang, F.J.; Myers, M.N. Theoretical and experimental characterization of flow field flow fractionation. *Anal. Chem.* **1976**, *48*, 1126.

59. Schimpf, M.; Caldwell, K.; Giddings, J.C. *Field Flow Fractionation Handbook*; Wiley Interscience, New York, NY, USA, 2000.

60. Bouby, M.; Geckeis, H.; Geyer, F.W. Application of asymmetric flow field-flow fractionation (AsFlFFF) coupled to inductively coupled plasma mass spectrometry (ICPMS) to the quantitative characterization of natural colloids and synthetic nanoparticles. *Anal. Bioanal. Chem.* **2008**, *392*, 1447–1457.

61. Wijnhoven, J.E.G.J.; Koorn, J.P.; Poppe, H.; Kok, W.T. Hollow-fibre flow field-flow fractionation of polystyrene sulphonates. *J. Chromatogr. A* **1995**, *699*, 119–129.

62. Benincasa, M.A.; Giddings, J.C. Separation and Characterization of Cationic, Anionic, and Nonionic Water-Soluble Polymers by Flow FFF: Sample Recovery, Overloading, and Ionic Strength Effects. *J. Microcolumn Sep.* **1997**, *9*, 479–495.

63. Ngo Manh, T.; Geckeis, H.; Kim, J.I.; Beck, H.P. Application of the flow field flow fractionation (FFFF) to the characterization of aquatic humic colloids: Evaluation and optimization of the method. *Colloid. Surf. A* **2001**, *181*, 289–301.

64. Henrist, C.; Mathieu, J.-P.; Vogels, C.; Rulmont A.; Clooots R. Morphological study of magnesium hydroxide nanoparticles precipitated in dilute aqueous solution. *J. Crystal Growth* **2003**, *249*, 321–330.

65. Phillips, V.A.; Kolbe, J.L.; Opperhauser, H. Effect of pH on the growth of Mg(OH)2 crystals in an aqueous environment at 60 °C. *J. Crystal Growth* **1977**, *41*, 228–234.

66. Rumyantsev, M.; Shauly, A.; Yiantsios, S.G.; Hasson, D.; Karabelas, A.J.; Semiat, R. Parameters affecting the properties of dynamic membranes formed by Zr hydroxide colloids. *Desalination* **2000**, *131*, 189–200.

67. Cho, H.-R.; Walther, C.; Rothe, J.; Neck, V.; Denecke, M.A.; Dardenne, K.; Fanghänel, T. Combined LIBD and XAFS investigation of the formation and structure of Zr(IV) colloids. *Anal. Bioanal. Chem.* **2005**, *383*, 28–40.